An explanation for USGS Station 6 record, 1979 Imperial Valley earthquake: a caustic induced by a sedimentary wedge

J. A. Rial, V. Pereyra and G. L. Wojcik

REPRINTED FROM
Geophys. J. R. astr. Soc. (1986) **84**:2, 257–278
PUBLISHED BY
BLACKWELL SCIENTIFIC PUBLICATIONS
OXFORD LONDON EDINBURGH BOSTON PALO ALTO MELBOURNE

Geophys. J. R. astr. Soc. (1986) **84**, 257–278

An explanation for USGS Station 6 record, 1979 Imperial Valley earthquake: a caustic induced by a sedimentary wedge

J. A. Rial* *C.F. Richter Seismological Laboratory, University of California at Santa Cruz, Santa Cruz, CA 95064, USA*

V. Pereyra and G. L. Wojcik *Weidlinger Associates, 620 Hansen Way, Suite 100, Palo Alto, CA 94304, USA*

Accepted 1985 June 17. Received 1985 June 17; in original form 1985 March 26

Summary. The largest earthquake-induced acceleration yet recorded occurred at the United States Geological Survey's (USGS) Strong Motion Array Station 6 during the 1979 October 15, Imperial Valley, California earthquake. This large acceleration (1.74 g, vertical component) is anomalously strong considering the low magnitude of the event ($M = 6.4$), and the fact that receivers in the immediate neighbourhood of Station 6 recorded much lower accelerations. Previous studies of the records by other investigators have suggested a number of explanations for the anomaly, several of which implicate the near-receiver geological structure.

We present a detailed time and frequency domain analysis of the acceleration records at Stations 6, 5, 7, 8 and Diff Array to suggest that the anomalous acceleration is the consequence of the focusing of the incoming body waves by the lens-like effect of the sedimentary wedge between Imperial Valley and Brawley faults. The analyses include a detailed comparison of observed particle motions between neighbouring stations. Narrow band-pass filtered particle motions at Station 6 reveal the interaction of multipath arrivals as well as the frequency-dependent interference between them. Three-dimensional ray tracing experiments confirm the fact that the faulted sedimentary wedge is capable of focusing *P*-waves near Station 6. The interpretation that best combines theoretical and observed results is that amplification was due to the formation of an elliptic umbilic caustic with focus near the surface.

Key words: caustics, focusing, strong ground motion, 1979 Imperial Valley earthquake

1 Introduction

The 1979 October 15, Imperial Valley earthquake was recorded by a large number of advantageously distributed strong motion stations, one of which (Array Station 6) recorded

* Present address: Geology Department, University of North Carolina at Chapel Hill, NC 27514, USA.

the largest earthquake-induced peak acceleration observed to date (1.74 g, vertical component). The detailed study and interpretation of this anomalously large acceleration is the subject of this paper. We base the analysis on the hypothesis that the observed large amplification and particle motions at Array Station 6 are consistent with the formation of a strong caustic under the station, induced by the lens-like effect of the sedimentary wedge formed by the Imperial Valley and Brawley faults. The philosophy behind this approach has been discussed previously (Rial 1984), and assumes that the commonly observed large fluctuations in acceleration and intensity of ground shaking are often a consequence of focusing and caustics formed when high-frequency (1–30 Hz) body waves propagate through irregularly shaped sedimentary basins. These basins, acting like deformed optical lenses, are capable of producing a complex network of patches and seemingly isolated pockets of anomalously large accelerations (or intensified damage) where the caustic intersects the ground surface. Results obtained in the present work extend this idea to include basins limited by faults, graben-like, and wedge-like structures.

Previous studies of the accelerograms at Imperial Valley Array Station 6 have attributed the large acceleration to amplification due to path effects (Mueller & Boore 1981; Hartzell & Helmberger 1982; Mueller, Boore & Porcella 1982; Boore & Fletcher 1982; Archuleta 1982; among others). Source effects have also been invoked as a possible alternative by Archuleta (1982) who proposes that rupture velocity exceeding *S*-wave velocity could have affected the *P*-wave radiation producing a forward-focused pulse in the direction of the recording site. Interpretations that support the existence of a path effect include near-surface reverberations due to high impedance contrast between dry and saturated sediments (Mueller *et al.* 1982), and the effect of a *PP*-wave type phase whose travel-time curve contains a cusp at the epicentral distance of Station 6 (Archuleta 1982). This author suggests that the maximum acceleration at Station 6 is due, in part, to the local site amplification proposed by Mueller *et al.* (1982), and in part to the *PP* phase, which also causes peak vertical accelerations larger than, or comparable to, either horizontal component at some other recording sites.

There are important features of the observed accelerograms at Station 6 that do not seem to be satisfactorily explained by those interpretations, namely the complex particle motions associated with the peak acceleration, and the peculiar spectral content of the signal. We discuss these features in detail in this paper and conclude that a more likely explanation is the focusing of *P*-waves. Results of time and frequency domain analyses of the records are consistent with theoretical predictions obtained by three-dimensional ray tracing in models of the geological structure under the station.

2 Data

Locations of the USGS Imperial Valley array stations and the surface traces of the Imperial and Brawley faults are shown in Fig. 1. The accelerograms we shall describe in most detail are from Stations 5, 6 and 7. The strong motion instruments at those sites were triggered by a small, precursory event so that the *P*-waves from the main shock were completely recorded (Porcella & Matthieson 1982).

In the present study, we are concerned primarily with the analysis of the first 4 s after trigger time. Interesting features in this interval are shown in Figs 2–5. In Fig. 2 the peak vertical acceleration at Station 6 is compared with corresponding arrivals at Stations 5 and 7. Also shown are the horizontal (radial and transverse) components of motion. At Station 6 the interval between 2 and 3 s after trigger time shows that the peak vertical acceleration occurs within a distinctive wavetrain that resembles a nearly monochromatic wavepacket,

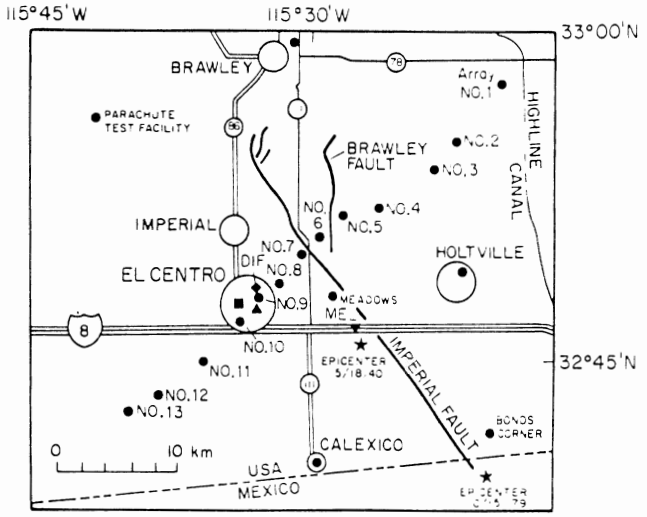

Figure 1. Area map of the southern Imperial Valley showing the surface traces of the Imperial Valley and Brawley faults and the location of strong motion instruments (from Porcella & Matthieson 1982).

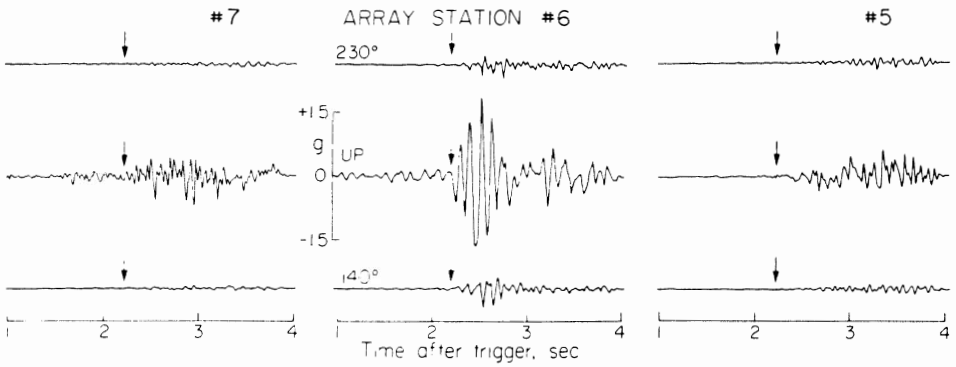

Figure 2. Vertical and horizontal components of the first arrivals (acceleration) of the Imperial Valley 1979 earthquake at El Centro Array Stations 5, 6 and 7. Arrows indicate the approximate arrival time of the main *P*-phase. Note the strong horizontal components at Station 6 at the time of the peak vertical acceleration (1.74 g).

accompanied by relatively large radial (140° component) and transverse (230° component) motions.

The peak vertical acceleration at Station 6 (1.74 g, uncorrected) shown in Fig. 2 is the largest earthquake-induced acceleration ever recorded. These characteristics are in sharp contrast with the records at the two closest stations, 5 and 7, only 1–2 km away. All three stations are essentially equidistant (27 km) from the earthquake's epicentre (see Fig. 1). Horizontal components at the three recording sites are oriented in the same directions, parallel and perpendicular to the known trace of the Imperial Valley fault. Stations 5 and 6 were triggered within 0.36 s of each other (Porcella & Matthieson 1982). No accurate trigger time is known for Station 7, although it is presumably within 0.5 s of the other two. In the following we shall refer to the main shock as the late event arriving about 2 s after trigger time (as opposed to the small precursory event), with an epicentre on the Imperial Valley fault, in the neighbourhood of that of the 1940 May 18 event. Hartzell & Helmberger

(1982) locate the main fault break very close to that point, 8 km south of Station 7 and about 6 km deep, although the exact location is strongly dependent on the velocity structure chosen. We find reasonable agreement with these values (11 km south of Station 6 and 8 km deep, see below) by using a non-linear velocity gradient and comparing computed and observed $S-P$ times.

In Fig. 3 the first 12 s after trigger time at Stations 6 and 7 are shown after low-pass filtering the accelerograms to attenuate frequencies higher than 0.5 Hz. This allows the transverse *SH* and radial *SV* phases to be clearly identified as separate arrivals from the *P*-wave. The main *S*-wave phases arrive 2.5 s after *P*. Also observable in Fig. 3 is that the polarities of the *P* and *S* arrivals are consistent with the expected radiation pattern of a right lateral strike-slip fault with one nodal plane passing between the two stations. It is important to notice that in the filtered accelerograms the *P*-wavetrain lasts for about 2 s, between 2 and 4.5 s after trigger time at Station 6 and approximately between 2.5 and 4. 5 s after trigger time at Station 7. At least for the first 1.5 s after its arrival, the *P*-wave does not appear to be contaminated by non-*P* phases.

Fig. 4 shows the horizontal particle motions that correspond to the first 1.5 s of the *P*-wave, as identified in Fig. 3. This time the original accelerograms were low-pass filtered to attenuate only frequencies higher than 25 Hz. The strong horizontal accelerations at Station 6 relative to Stations 5 and 7 are clearly evident. As discussed in detail below, this evidence strongly suggests that the geological structure under Station 6 may not be composed of horizontal layers. In fact, the polarizations observed imply that, if the signal is a *P*-wave, energy is arriving from different directions not contained in the plane of incidence, i.e. that multipathing and therefore interference phenomena may have affected the *P*-wave at Station

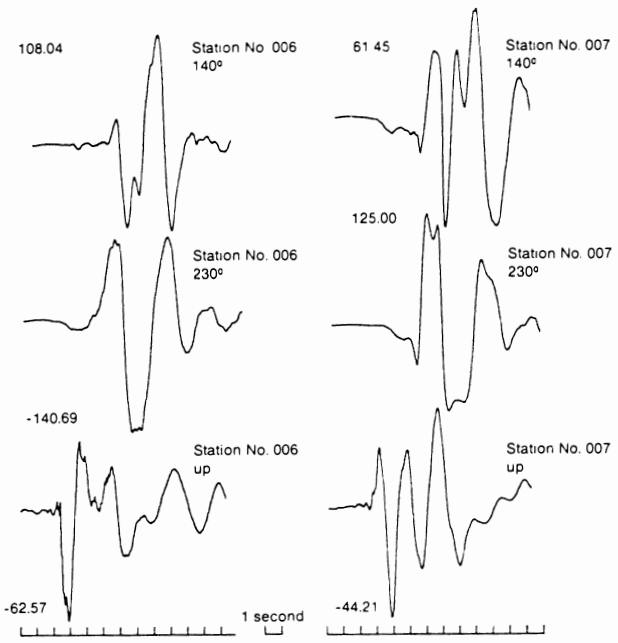

Figure 3. Accelerograms of the 1979 Imperial Valley earthquake at Array Stations 6 and 7. The original traces have been low-pass filtered to identify the *P*, *SV* and *SH* arrivals better (Filter's corner frequency at 0.5 Hz). All traces are aligned at trigger time. Note the well-defined *SV* (140° component) and *SH* (230° component) arrivals 2.5 s after the *P*-wave. Maximum accelerations of the filtered records (in g) are shown for each trace.

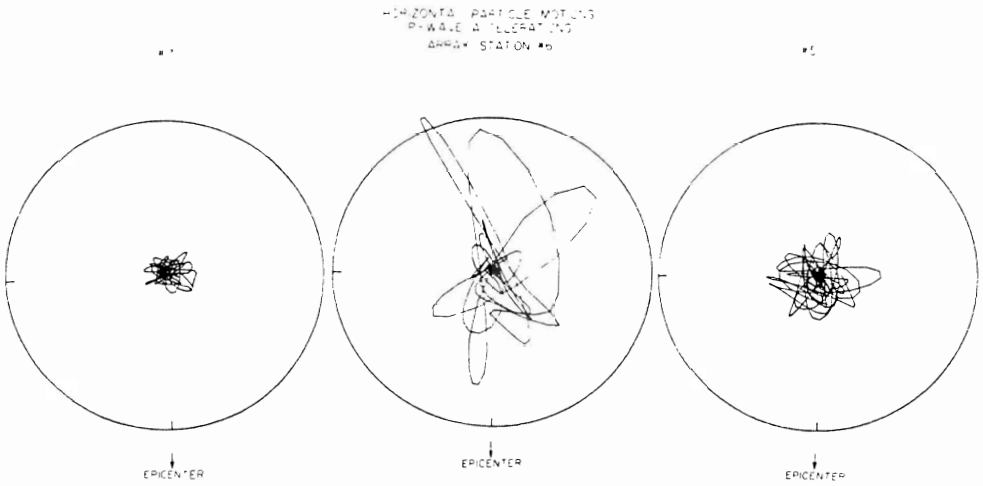

Figure 4. Horizontal particle motion diagrams (planographs) of the first 3.25 s after trigger time at Stations 5, 6, and 7 (see Figs 1 and 2 for reference). The original records were low-pass filtered to attenuate frequencies higher than 25 Hz. Most of the observable motions occur between 2 and 3.5 s after trigger time. The radius of the circle represents 0.36 g.

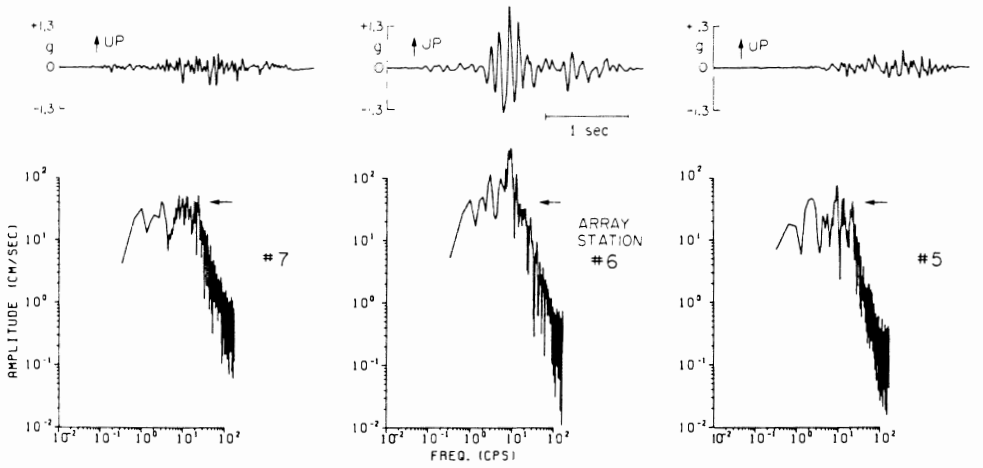

Figure 5. Fourier spectra of the vertical components of acceleration at Stations 5, 6 and 7 in the time interval of Fig. 2. Note that in the 1–10 Hz range the spectral amplitude at Station 6 increases nearly as the first power of frequency, whereas at the other stations it is flat in this range. The arrows are for easy reference.

6. This could account for the strong vertical amplification and the wavepacket appearance of the signal shown in Fig. 2.

Another interesting aspect of the record at Station 6 is shown in Fig. 5. Here we compare the Fourier amplitude spectra of the vertical components shown in Fig. 2. The uncorrected accelerograms for the interval shown were interpolated at 300 sample s^{-1}, detrended and high-pass filtered to attenuate periods longer than 20 s. The selected time interval was then cosine windowed and the FFT algorithm applied to the resultant time series. The important point to be noticed in Fig. 5 is that within the range 1–10 Hz the spectral amplitude in Station 6 increases non-linearly with frequency, whereas at Stations 5 and 7 it is flat in this

range. This is an important point which we discuss below in detail, because such frequency-dependent behaviour may be indicative of strong focusing.

3 Particle motion analyses

In Fig. 6 observed planographs (particle motion diagrams) for the first 1.5 s of the *P*-wave are shown for Stations 7, 6, 5 and 8. The time intervals for all planographs were selected such that, within the uncertainties of the absolute timing at some stations, the same time interval after the first arrival is compared at all receivers. In general, for the stations named above, the first arrivals can be detected without too much difficulty (cf. Fig. 2). Of course, by first arrivals is meant those of the main shock. The original records were low-pass filtered to eliminate frequencies higher than 25 Hz.

The polarization observed in the vertical/radial and vertical/tangential planographs of Fig. 6(a) (Station 7) are consistent with a *P*-wave incident at a steep angle under the station. Note that the direction towards the source is to the left of the figure. The overall characteristics of these particle motions may be considered as normal, namely that they are consistent with a *P*-wavetrain that shows no obvious path effects. Comparison with planographs in Station 6 (Fig. 6b) reveals much of the anomalous character of the accelerograms at this station, as evidenced by large vertical acceleration with strong horizontal components. At Station 6 the horizontal polarizations of the first arrivals indicate that energy arrives from the west (lobe 1), the south-east (lobe 2), the south (lobe 3) and the south-west (lobe 4) of the station. This sequence of polarizations suggests multipathing, and their orientation, as will be shown below, can be explained by the refraction of *P*-waves through the Imperial Valley and Brawley faults. Thus, if the first arrivals at Station 6 are *P*-waves, as their timing implies, the observed differences in horizontal polarization between Stations 6 and 7 are difficult to explain unless there are dipping interfaces under and to the west and east of Station 6 capable of bending the approaching rays, thus drastically changing their horizontal polarization. The geological structure under this area proposed by Fuis *et al.* (1982) can be seen to consist of a wedge-like structure limited by the two faults in a way that could make the *P*-wave rays converge towards the surface and eventually coalesce and focus. The lens-like (or prism) effect of the wedge would also explain why strong vertical arrivals are recorded in a direction that is almost nodal for *P*-waves.

In the horizontal planograph of Station 6 in Fig. 6(b), the arrows and the number sequence indicate the sense of motion and relative timing of the different orbits. The time interval from points 1 to 4 is only 0.25 s, so that it is difficult to interpret the different orientations of the lobes as a result of the motion of the rupture front with respect to the station which in that time (assuming a rupture velocity of 3 km s^{-1}) must have moved less

Figure 6. Particle motion diagrams (planographs). (a) Imperial Valley Array Station 7. The time interval represented is 1.5 s, i.e. 2–3.5 s after trigger time, corresponding to the main *P*-wave arrival from the earthquake. Frequencies higher than 25 Hz have been filtered out. The projection planes are from left to right, radial/tangential, tangential/vertical and radial/vertical. The epicentre is to the left of the figure (140° component). For this and (b) and (c) the horizontal particle motions are normalized to 0.36 g, and the vertical particle motions to 0.7 g, a convenient value to compare among stations (see b). (b) As (a) for Imperial Valley Array Station 6. On the top row the vertical planographs are normalized to the maximum vertical acceleration (after filtering out frequencies higher than 25 Hz). On the bottom row the normalization is as in (a). The particle motion lobe labelled 1 corresponds to the arrival of the peak vertical acceleration. Lobes 2, 3, 4 follow in temporal sequence. Arrows indicate sense of motion. (c) Same as for (a) Array Stations 8 (top row) and 5 (bottom row). Normalization and projection conventions are as in (a). Stations 5 and 6 are located east of the Imperial Valley fault, Stations 7 and 8 west of it.

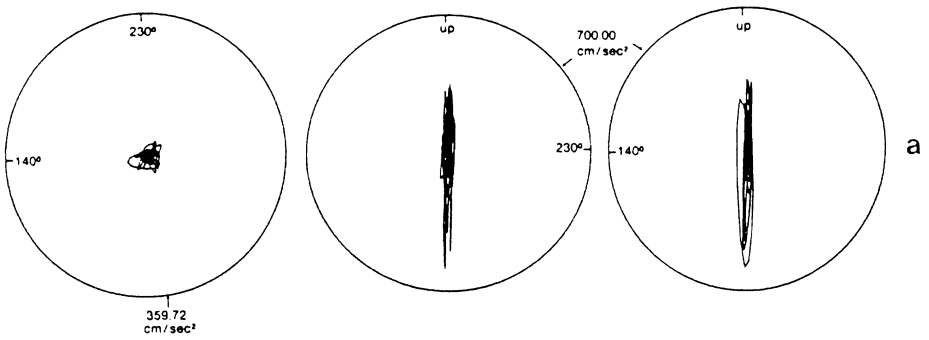
230°
140°
359.72
cm/sec²
up
230°
700.00
cm/sec²
up
140°

a

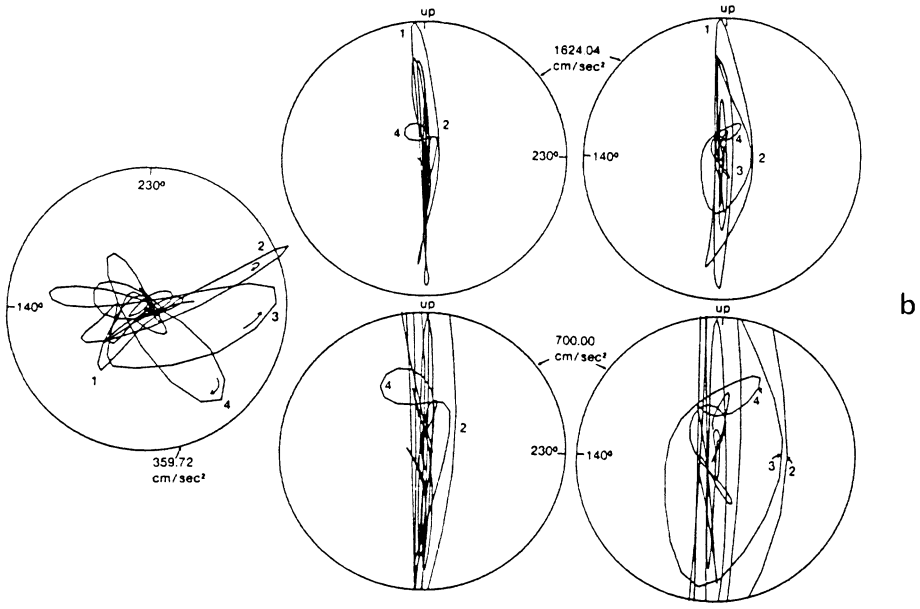
230°
140°
359.72
cm/sec²
up
1
2
4
230°
1624.04
cm/sec²
up
1
4
2
140°
3
up
4
2
230°
700.00
cm/sec²
up
4
140°
3
2

b

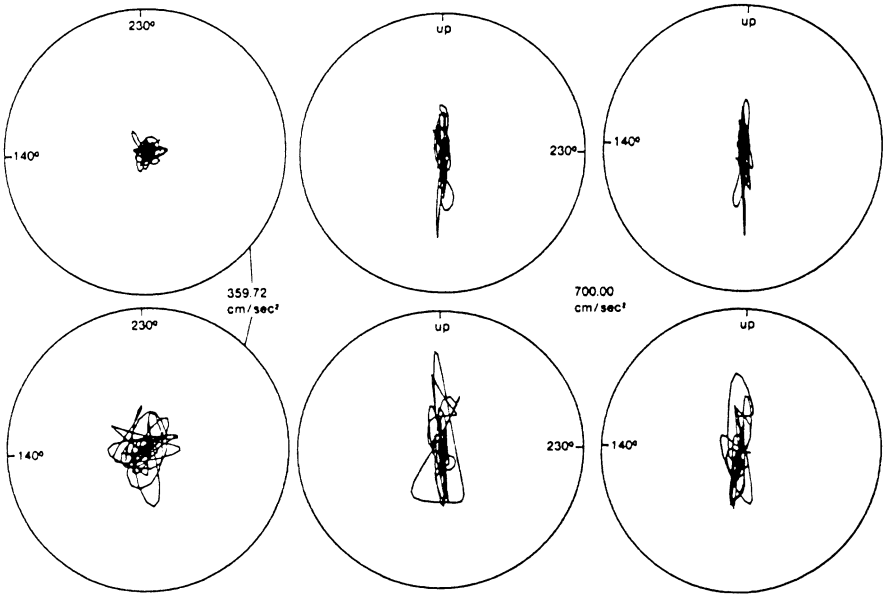
230°
140°
359.72
cm/sec²
up
230°
700.00
cm/sec²
up
140°
230°
140°
up
230°
140°

c

than 1 km in the NW direction, the proposed rupture direction for this event (Hartzell & Helmberger 1982). It is possible that some of the horizontal motion in Station 6 is the result of the arrival of *SV*-waves converted from *P* at a curved interface very close to the surface, so that for certain frequencies refracted *P* and converted *SV* phases interfere constructively and produce the strong amplification. However, invoking these arrivals does not appear necessary, since, as shown below (cf. Figs 11–16) the refracted *P*-wave alone can account for the observed polarization. Also a detailed analysis of the particle motions (cf Fig. 8) indicates that in this time interval all arriving energy shows *P*-wave polarization. Direct *SV*-waves from the source could not cause the horizontal motions because, as shown in Fig. 3, they arrive much later in the record.

Fig. 6(c) displays planographs for Stations 5 and 8 that can be used for comparison with the two just discussed. It may be noted that stations east of the Imperial Valley fault (Stations 5, 6) show, in general, relatively stronger horizontal components of the *P*-wave than those to the west (Stations 7, 8). These characteristic differences are also observed when comparing (not shown) Stations 3, 4 (east) and 9, Diff Array (west).

4 Spectral ratios and filtered particle motions

We have so far presented evidence that suggests the presence of non-planar (or at least dipping) interfaces under Station 6 and thus the inference that the observed amplication may be due to focusing. However, the complexity of the signals makes the interpretation difficult and a more detailed knowledge of the local structure is necessary in order to be able to produce realistic synthetic accelerograms. An approach that provides results simpler to interpret consists of narrow band-pass filtering the signals in such a way that the resulting accelerogram and particle motions can be viewed as an almost monochromatic Fourier component of the original accelerogram. For this purpose, we used a combination of low-pass and high-pass, fifth-order Butterworth filters with corner frequencies at the selected frequency to be analysed. The maximum acceleration for each selected frequency within the first 3.5 s of the record were thus obtained for Stations 5, 6, 7 and Diff Array. Care was exercised so that the time intervals selected were equivalent in all four stations. This was accomplished by signal cross-correlation and filtering, as shown in Fig. 3. Acceleration ratios were also computed dividing the maximum accelerations at Station 6 by the corresponding ones at the other sites. The resultant maximum accelerations and acceleration ratios are displayed in Fig. 7 as a function of centre frequency of the band-pass filter. In Fig. 7, the resulting curves are shown in pairs, corresponding to stations east and west of the Imperial Valley fault. The slight differences among the response curves of Stations 5, 7 and Diff Array probably reflect the existence of different surficial structure across the fault, which is consistent with observed differences in horizontal particle motions between stations to the east and west of the Imperial Valley fault mentioned above. Relative to Station 6 (Fig. 7) in the frequency range 1–15 Hz, the spectral ratios of Stations 5, 7 and Diff Array are very similar, suggesting that the response of Station 6 is nearly independent of the relatively minor changes in crustal structure from west to east. An essential feature in Fig. 7 is that independently of the recording station (Stations 5, 7, Diff Array) the relative maximum accelerations of the band-pass filtered traces at Station 6 grow as a fractional power of frequency in the range 1–10 Hz, beyond which strong attentuation appears to occur at Station 6 and consequently the acceleration ratios suddenly and sharply drop. The largest amplification occurs between 8 and 10 Hz, as can directly be observed in Fig. 5. This power-of-ω dependence is characteristic of focusing, which we shall discuss below.

As discussed above, the particle motion diagrams at Station 6 are strongly suggestive of

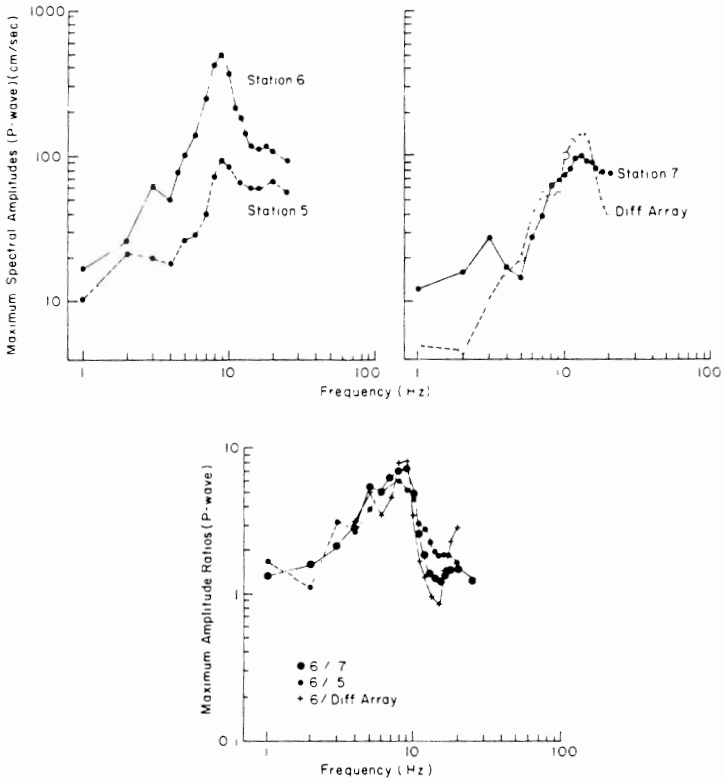

Figure 7. Observed *P*-wave maximum accelerations (top) and spectral ratios (bottom) as a function of frequency for Stations 5, 6, 7 and Diff Array. Notice that for stations east of the Imperial Valley fault (Stations 6 and 5) the response curves are similar, and different from those at Stations 7 and Diff Array located west of the Imperial Valley fault. Relative to all the other stations, Array Station 6 shows a consistent increase of spectral maximum acceleration in the range 1–10 Hz.

the fact that *P*-waves arrive at the site from directions other than those contained in the plane of incidence. Fig. 8(a, b) shows particle motion diagrams of the band-pass filtered accelerograms at Station 6 for the same time interval 2–3.5 s after trigger time that, as previously discussed, corresponds to the amplified arrival. The resulting diagrams show the behaviour of individual Fourier components of the trace. Assuming that the principle of superposition is applicable, each filtered planograph can be interpreted as if the source itself was monochromatic of that frequency. The frequencies selected for study (Fig. 8) range from 7 to 14 Hz in steps of 1 Hz. Some of the resulting filtered accelerograms are shown in Fig. 9. The sequence of planographs is most informative when seen as a function of increasing frequency. In all diagrams the radial/tangential, the vertical/radial, and the vertical/tangential particle motion projections are displayed from left to right. For convenience in the interpretation, the horizontal planographs are now oriented such that the direction to the top of the page is the direction towards the epicentre (140° component). As a function of frequency all three projections show particularly clear rotation of the polarization axes (defined here as the direction of the longest axis of the ellipse-like orbits of the particle motion). These rotations are clearly observed on all projection planes. For instance, on the vertical/radial planographs at 8 Hz, the polarization axis is oriented away from the source for the compressional part of the pulse (Fig. 8a). At

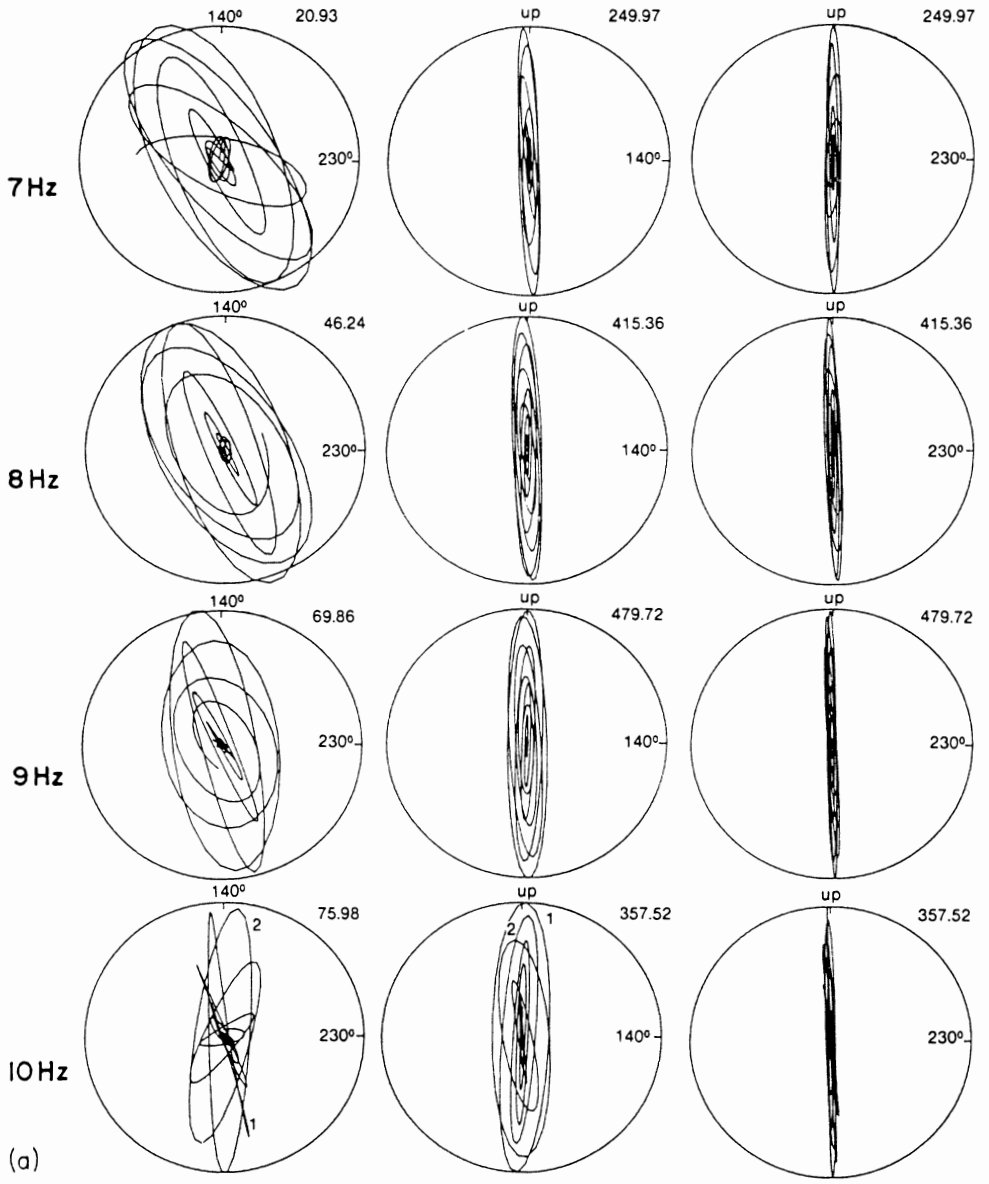

Figure 8. Particle motion diagrams of the *P*-wave at Station 6 plotted as a function of frequency in the range 7–14 Hz. The time interval represented is 2–3.5 s after trigger time. The interpretation given to this sequence of planographs is explained in the text. The original traces were band-pass filtered with a fifth-order Butterworth filter centred at the indicated frequencies.

9 Hz the polarization axis is nearly vertical. With increasing frequency it rotates clockwise such that at 14 Hz the polarization is towards the source when compressional. At the same time, splitting of the orbits is observed starting at about 10 Hz. In fact, at 14 Hz two distinct polarization axes are observed that can also be seen on the horizontal and vertical/tangential projection planes. Split orbits are numbered 1 and 2, the figures indicating relative arrival times. That is, orbits 2 occur after all motion in orbits 1 has ended.

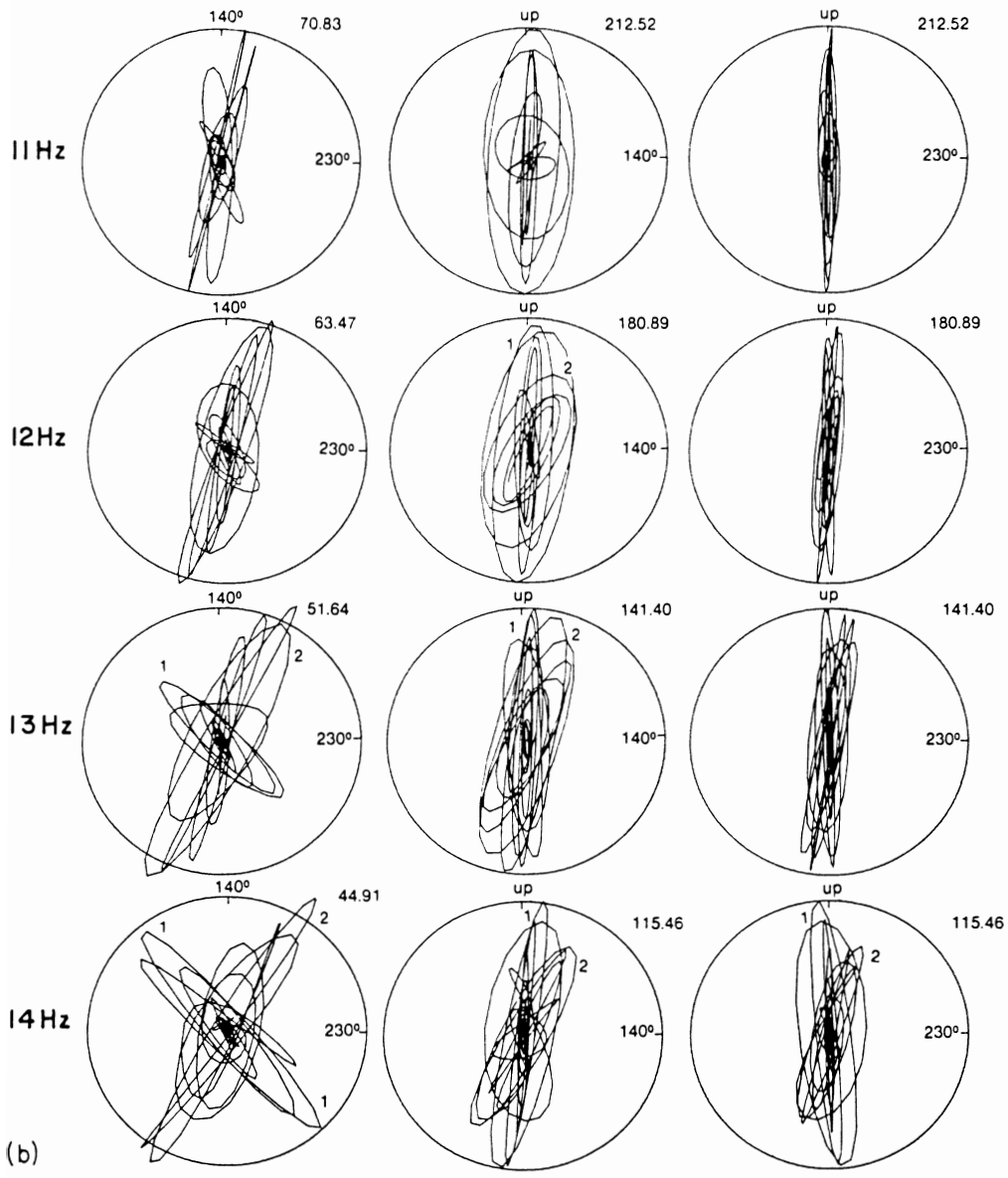

Figure 8 – *continued*

We interpret the sequence in Fig. 8(a, b) as follows: The *P*-wavetrain at Station 6 arrives between 2 and 3.5 s after trigger time. At least two independent arrivals coalesce at the surface and, for harmonic components of frequencies between 9 and 10 Hz, constructive interference occurs. The two 'rays' can be observed as independent arrivals (not interfering) for frequencies higher than 11 Hz. Particularly at 14 Hz (Fig. 8b), the horizontal polarizations of the two rays indicate that they arrive from the sides of the incident *P*-wave plane, possibly after being deflected by the Imperial and Brawley fault planes. Since Station 6 is located very close to a predicted node of *P*-wave radiation, it is possible that these two rays would have never arrived at the station had there not existed a deflecting structure such

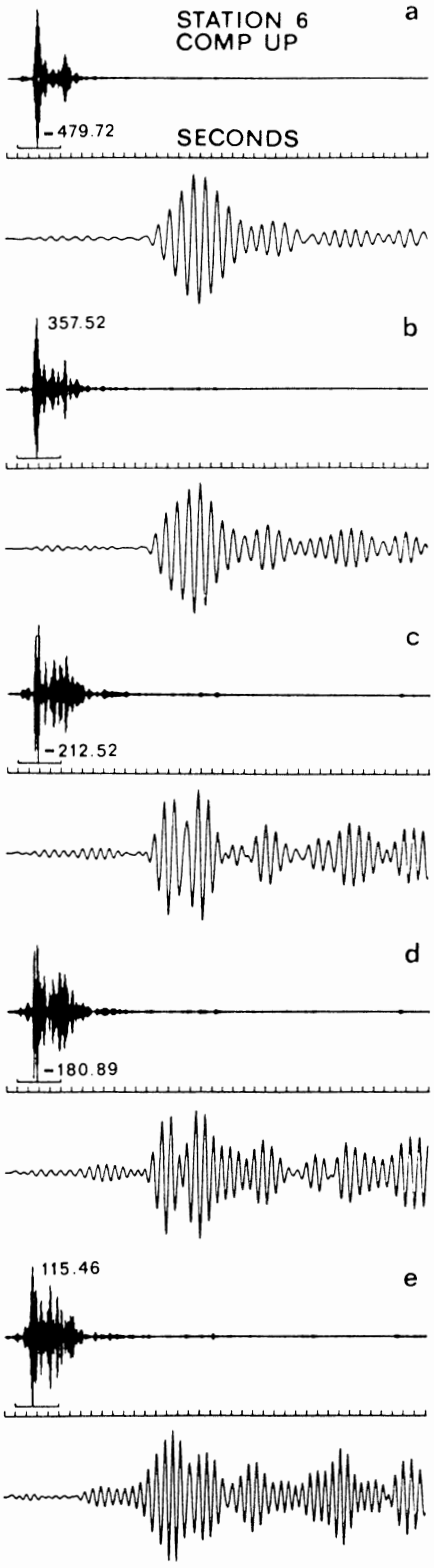
STATION 6
COMP UP
a
-479.72
SECONDS
357.52
b
c
-212.52
d
-180.89
115.46
e

as the Imperial/Brawley graben-like wedge that made them coalesce and focus. The interference process of the two coalescing rays can be seen clearly in the filtered traces of Fig. 9. Thus, the particle motion orbit rotations appear to correspond to the interference between at least two separate arrivals, whose presence is evidenced by the splitting of the orbits when the frequency is high enough and their interference is weakest. Also, between 9 and 11 Hz the horizontal orbits rotate crossing the direction towards the epicentre (140° component) at 10 Hz, where the orbits are almost purely radial. This suggests that transverse components of the converging rays cancel each other, whereas the radial components constructively interfere.

It can be shown that between 8 and 10 Hz the tangential component of the *P*-wave at Station 6 has nearly the same amplitude as the *S*-wave and at 11 Hz it is less than half that of the *S*-wave. At Station 7, in contrast, the transverse component of the *P*-wave is one-fourth to one-third of the *S*-wave in the range 8–11 Hz.

At frequencies lower than 8 Hz, most of the energy seems to arrive from a point slightly to the east of the epicentre, and the vertical/radial orbit is up when away. At these relatively low frequencies, diffraction effects are probably important and soften the focus. Also, the radius of curvature of the deflecting surface may already be of a magnitude close to the incident wavelength so that the amplification decreases, and the relief of the interface becomes smoother to the incoming wavelengths.

Checks on the reliability of the particle motion orbits were performed by analysing the stability of the horizontal particle motion orbits of the aftershock recorded at Station 6 about 35 s after trigger time, whose *P*- and *S*-waves are particularly simple. Especially at frequencies higher than 10 Hz a small misalignment on the initial time in any of the three components of motion may induce spurious phase relations between the components and thus false rotations. The polarization axes of the *P*-wave particle motions of the aftershock were seen to remain stable from 9 to 20 Hz with only small (2–3°) oscillations around the direction N45W–S45E, the *S*-wave orbits remaining perpendicular to that direction.

It should be clear that the anomalously large horizontal amplitudes of the *P*-wave at Station 6 and the clearly developed linear polarizations observed (Fig. 6b) provide justification for the filtering experiment shown in Fig. 8. Similar experiments on Stations 5, 7 or 8 would not provide additional information. The horizontal amplitudes at Stations 7 and 8 are too close to the noise level and show no preferred polarization. The horizontal/vertical amplitude ratio is 1:10 or smaller. At Station 5 the horizontal components are somewhat larger relative to the vertical but do not show any particular preferred polarization (a seemingly large radially polarized arrival is a late-arriving, non-*P* phase).

5 Reverberation or focusing?

Mueller *et al.* (1982) interpret the amplification at Station 6 as due to reverberation in the flat-layered, near-receiver structure. Their analysis does not consider the observed facts discussed above, especially the complex horizontal polarization at Station 6. The main emphasis of their work is the relative spectral amplitudes between Stations 5, 7 and 6. They compare spectral ratios computed for a flat-layered receiver structure with those observed.

Figure 9. Selected band-pass filtered traces of the vertical accelerogram at Station 6. (a) Centre frequency of filter at 9 Hz. (b) Centre frequency of filter at 10 Hz. (c) Centre frequency of filter at 11 Hz. (d) Centre frequency of filter at 12 Hz. (e) Centre frequency of filter at 14 Hz. The lower trace in each case is a blow-up of the (marked) 4 s interval on the upper trace. Note the separation of the *P*-wave train into two distinct phases for frequencies higher than 10 Hz.

Their model, however, predicts resonant peaks to occur at 12 and 15 Hz, depending on the velocity assigned to the surface layer, whereas the predominant frequency of the amplified signal is centred between 8 and 10 Hz (Figs 2 and 5). The reason for this discrepancy is not clear from their analysis. We do not object to the possibility of resonances being produced by the thin (5–8 m) low-velocity layer (0.4–0.5 km s^{-1}) found at the surface, but this does not seem to be related to the wavepacket containing the 1.74 g peak acceleration which clearly (Fig. 5) shows very little spectral energy in the 12–15 Hz range.

In a related study, Boore & Fletcher (1982) show *P*- and *S*-wave spectral ratios of local events recorded at the sites of Stations 6 and 7 of the Imperial Valley array (see their fig. 83) that show narrow resonant peaks at 12 Hz for *P*-waves and 4 Hz for *S*-waves. No indication of resonance is found in the range 8–10 Hz. Also, Mueller *et al.* (1982) give special attention to the fact that a section of the coda recorded at Station 6 is also amplified with respect to the corresponding sections of the coda at receivers 5 and 7. It is important to note, however, that within the coda section selected (20–30 s after trigger) at least one aftershock is clearly recorded at Station 6, arriving 26 s after trigger. The beginning of their selected coda section is also within 1 s of the *P*-wave of an earlier aftershock that arrives 19 s after trigger (see Fig. 10). The corresponding coda sections at Station 5 or 7 also show these aftershocks but the signals are much noisier than at Station 6. Thus, the presence of these aftershocks makes it possible to explain the observed coda amplification also as focusing, as source effects or as a combination of both.

6 Interpretation of the data: ray tracing in a 3-D wedge

The arguments put forward so far to support our idea that focusing and multipathing are responsible for the largest peak acceleration so far observed in earthquakes can be substantiated by ray-tracing experiments.

To calculate the ray trajectories from the source to Station 6 in Imperial Valley, it is necessary to model the complex geological structure formed by the intersecting Imperial Valley and Brawley faults. According to published models (Fuis *et al.* 1982) the geological structure underlying Station 6 is a 3-D sedimentary wedge limited by the two faults. The seismic wave velocity distribution includes a strong, positive gradient near the surface which decreases gradually with depth. The velocity contrast between the (relatively low velocity) sediments inside the wedge and those outside is not well-known but can be inferred to lie between 1/1.3 to 1/2.0 from refraction profiles obtained by Fuis *et al.* (1982) and from the surficial wave velocity contrast across the fault traces. The sediments within the wedge have been offset from those outside due to downdip displacements along both faults. Thus, in the area close to the intersection of the two faults, i.e. near Station 6, the geology may be described as a graben-like structure, the sedimentary wedge being the subsiding block. Dips of the Imperial and Brawley faults are known within 10° (Fuis 1984, private communication) in the area surrounding Station 6. Both faults are steeply dipping, with angles between 70 and 80°. The strike of the faults at depth seems to change little from measurements at the surface (140° for Imperial Valley and 180° for Brawley, see Fig. 1). Since both faults are potentially capable of deflecting approaching rays, to understand the possible ray trajectories, it is necessary to use a 3-D ray tracing scheme.

We used two methods to trace rays through models of the Imperial Valley wedge. One solves the ray trajectory equations as a two-point boundary value problem, i.e. with prescribed source and receiver locations, one or more rays are obtained that join these two boundary points (Pereyra 1984). The other method uses the two-point code in a 'shooting' mode where the source location, initial ray direction and final interface are prescribed. Both

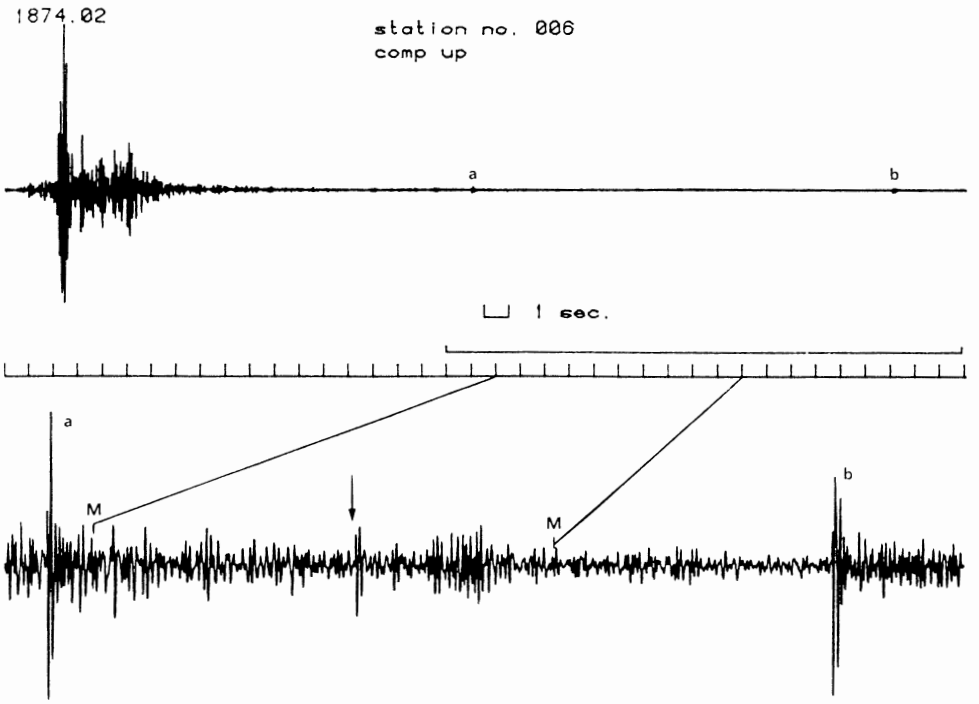

Figure 10. Band-pass vertical component at Station 6 showing the interval analysed by Mueller *et al.* (1982) marked MM. Observe the *P*-wave arrival (marked with an arrow) of a small aftershock and the fact that the MM coda section begins 1 s after the *P*-wave arrival of a stronger aftershock (marked a).

methods allow 3-D ray tracing in heterogeneous, piecewise continuous media. Receivers are distributed on the surface along a line or grid. An approximate trajectory initializes the algorithm which uses a Newton iteration to converge to the nearest Fermat ray. Once a ray is found, its trajectory is used again to initialize the code for the ray arriving at the next station on the grid. The same set of receiver locations can be prescribed more than once with different initial rays to obtain all possible solutions (multipaths) to a given station. At any point on a given ray the travel time, ray length, ray parameters and ray amplitudes can be computed. The method has been successfully applied to ray tracing in sedimentary basins of general form (Pereyra & Rial 1981).

Figs 11–15 illustrate some of the 3-D ray tracing experiments carried out using the above methods. Fig. 11 shows a perspective view of the area near Station 6 and two sets of rays obtained using the two-point method. The figure shows rays arriving at a line of receivers located near the intersection of Imperial Valley (IV) and Brawley faults, as seen from an elevated point SW of the intersection. The reference cube is 4 km on a side and stations are distributed along a line parallel and shifted 1 km to the east of the IV surface trace. The set of rays on the left are refracted at depth by IV fault and those to the right by the Brawley fault. Selection of a 75° dip for both faults was made after several models with dips within plus or minus 5° did not show important differences in the resultant ray paths from those shown. The (point) source is located 10 km to the south of the closest station, 8 km below the surface and on the Imperial Valley fault. This gives a *P*-wave travel time to Station 6 of 3.1–3.3 s (depending on the velocity model), which is consistent with the estimates of Hartzell & Helmberger (1982) of the source's location. Several different source locations

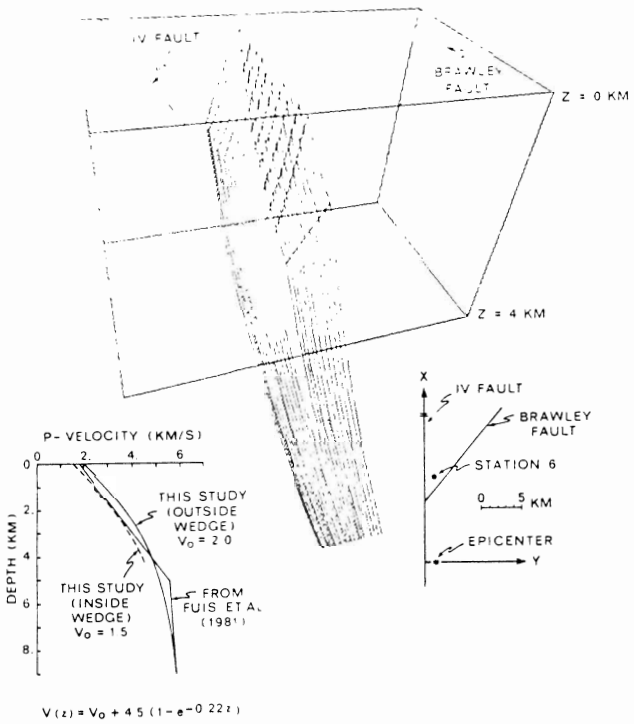

Figure 11. 3-D perspective view of the interaction of seismic rays with the preferred model of the wedge-like structure limited by the Imperial Valley (left) and Brawley (right) faults. The line of receivers is parallel to the Imperial Valley fault. The (point) source is located 10 km to the south of the closest station and 8 km below the surface. Both faults have a dip of 75°. The velocity structure is given by the equation in the inset with $V_0 = 1.5$ and 2 km s^{-1} for the surface velocity inside and outside the wedge, respectively. $K = 4.5$ km s^{-1} and $\alpha = 0.22$. Z is the depth from the surface. Station 6 would be located near the third receiver from the front. The two-point algorithm has been used to obtain all Fermat rays arriving at the prescribed stations (see text for details). In this and in the following figures, distances in kilometres are referred to the Cartesian coordinate system shown (no vertical/horizontal scale exaggeration).

were tested around a depth of 8 km and between 10 and 12 km south of Station 6. The resultant pictures are similar to that in Fig. 11, i.e. the multipathing and focusing occur in all cases, only the arrival times change.

In Fig. 11, Station 6 would be located near the third receiver from the front. Between the fourth and fifth stations from the front the two rays arrive simultaneously. The rays refracted by Brawley fault arrive first at the closer stations and last at the far ones. The largest travel-time difference between pairs of rays is only 100 ms for the model depicted in Fig. 11. This indicates that a cusp in the travel-time surface (a caustic line) must be close to the line of receivers. It is shown below that this is indeed the case (Fig. 15). The velocity structure in the area is simulated by an appropriate exponential function (see Fig. 11) with parameters V_0, K and D, where V_0 represents the wave velocity at the surface. The parameters that fit published values (see, e.g. Hartzell & Helmberger 1982; Fuis *et al.* 1982) are $V_0 = 2$ km s^{-1} outside the wedge and 1.5 km s^{-1} inside; $K = 4.5$ km s^{-1} and $\alpha = 0.22$. The non-linear form of the depth-dependent velocity is best suited to fit the strong velocity gradient of the first 5 km and its decrease with depth. Linear velocity gradients were also

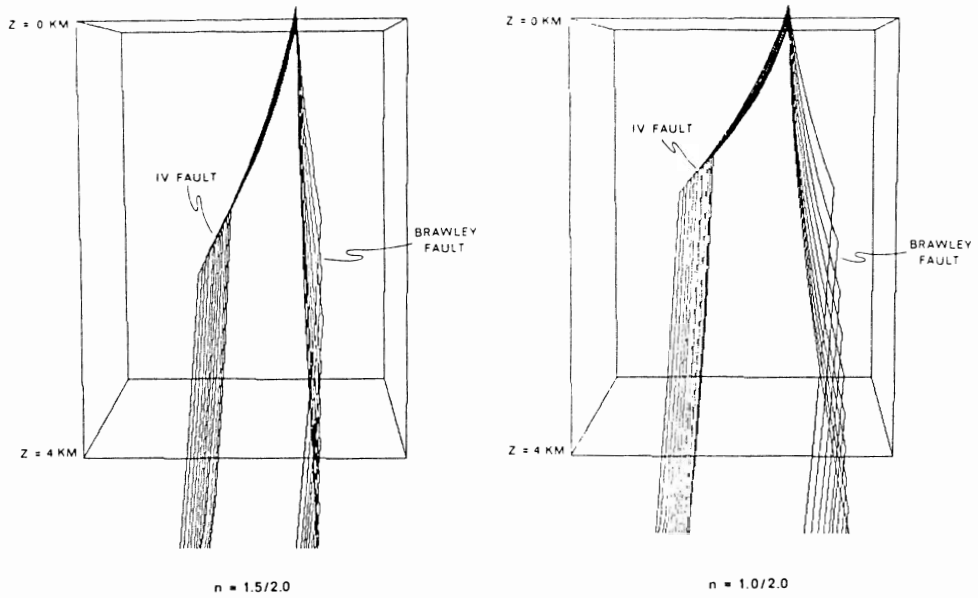

Figure 12. (a, b) As Fig. 11, now view from the epicentre. The effect of changing the refractive index across the faults is clearly seen. (a) V_0 = 1 km s^{-1} for the surface velocity inside the wedge and 2 km s^{-1} outside. (b) The preferred model (Fig. 11) is shown that corresponds to a refractive index across the faults, of 1.5/2.0.

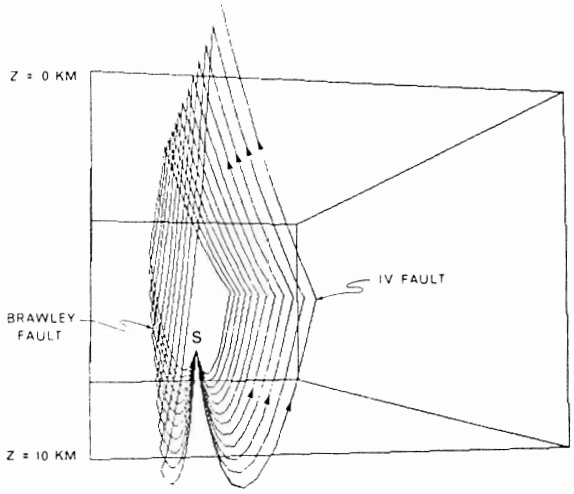

Figure 13. Perspective view of rays in the wedge looking toward the source. The velocity gradients are linear with depth at all depths, and the source is now 10 km further south than in Figs 11 and 12. The ray picture is, however, entirely similar to the previous ones: Two families of rays refracted by the Brawley and Imperial faults eventually converged at the Earth's surface along a line of receivers parallel to IV fault.

used, as well as different values of the refractive index across the faults with results qualitatively similar to those shown in Fig. 11. In Fig. 12 the effect of changing the velocity contrast is shown on a perspective view of the model in Fig. 11 as seen from the epicentre. In Fig. 13 the view is towards the source (labelled S).

Fig. 14 is again the model in Fig. 11 as seen from above. The approximate location of Station 6 and the caustic intersection with the line of receivers are shown. The top diagram

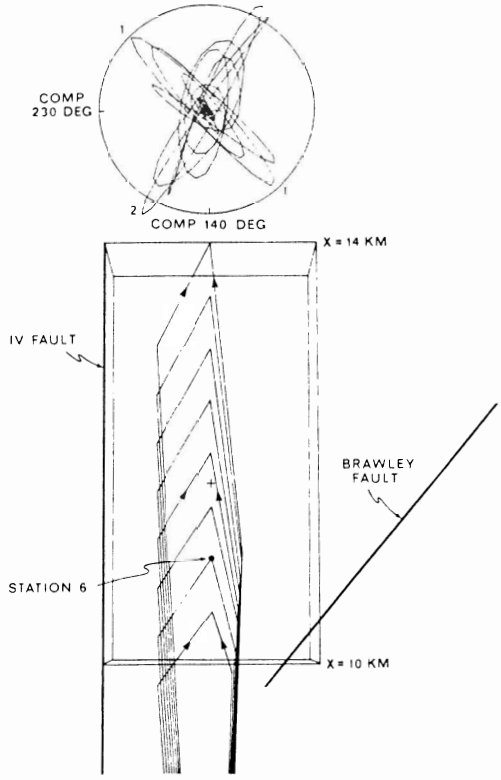

Figure 14. As in Fig. 11, now viewed from above. The ray tracings show the predicted orientation of the horizontal *P*-wave polarizations. The observed polarizations (see Fig. 9) are shown for comparison. The symbol (+) indicates the location at which the travel times of the two rays coincide (caustic point).

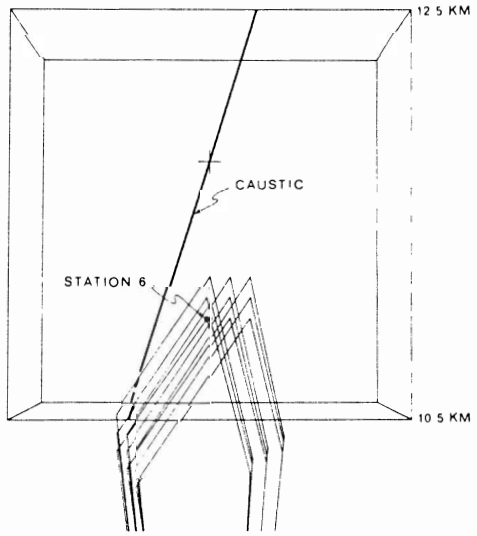

Figure 15. Trace of the caustic in the neighbourhood of Station 6. The fine mesh used for the receiving stations allowed the computation of the relative amplitudes associated to the two ray families.

is taken from the horizontal particle motion plots of Fig. 8 (14 Hz). The close agreement between the observed particle motions and the horizontal projection of the traced rays is very suggestive indeed. The sequence of arrivals of the observed particle motions is also in agreement with the calculated since, for stations closer to the source than the caustic point (+), the rays refracted through Brawley Fault arrive first. However, the calculated arrival time between the two rays at Station 6 is only 50 ms, in contrast with about 250 ms measured from the filtered records of Fig. 10. This discrepancy can nevertheless be made to disappear by slight modifications to the velocity structure of the model and/or the geometry of the faults. Also, the angle of arrival of the ray refracted by the Brawley fault in the model could be made to coincide exactly with that of the observed polarization by slightly modifying the strike of the fault at depth by a few degrees or by moving the epicentre a few hundred metres to the east, or by a combination of both. The uncertainties in the local geology would accommodate these modifications comfortably enough.

Fig. 15 shows a closer look at an area surrounding Station 6 and the local intersection of the caustic surface with the ground surface. Ray theoretical amplitude calculations show that the amplitudes of both families of refracted rays in the neighbourhood of Station 6 are of comparable magnitude.

7 The elliptic umbilic caustic

Figs 11–15 show the results of ray tracing in the simplest possible 3-D model of the structure underlying Station 6. However, the possibility of more than two arrivals converging at Station 6 within the time interval shown in Fig. 2 cannot be ruled out (see, e.g. Figs 6, 9 and 15). This may happen if the wedge model is slightly changed, as shown in Fig. 16. The intersection of the two faults is no longer a line and the wedge is simulated by a surface given by

$$z(x, y) = H\{1 - 9[x^2 + (y/2)^2]^2/L^2 + 6\sqrt{3}[x^3 - 3x(y/2)^2]/L^3\} \quad (1)$$

where the parameters H and L are shown in Fig. 16, and z is the depth from the surface. This equation is slightly modified from that used by Berry, Nye & Wright (1979) to study the canonic form of the elliptic umbilic caustic surface. The ray tracings in Fig. 16 show how a section of the surface given by (1), which has been made to fit closely the estimated geometry of the wedge under Station 6, produces an umbilic caustic with its highest singularity or focus close to the surface, near the location of Station 6. The 3-D canonic form of the elliptic umbilic is also shown in Fig. 16. The velocity structure as a function of depth, the local dimensions and geometry of the wedge (except near and at the intersection of the two faults) are basically the same as in the previous model. The essential difference between the two models is just that with direct rays being refracted into the wedge across the intersection of the faults, more rays interact, resulting in stronger focusing. There is justification to try the model described by equation (1) in that the behaviour of the spectral amplitude at Station 6 (see Fig. 8) relative to neighbouring stations may be explained by a stronger caustic than that produced by the interference of two rays. The predominant frequencies in the signal recorded at Station 6 (see Fig. 2) are in the range 4–10 Hz. The spectral ratios in Fig. 7 (see also Fig. 5) show that, with respect to the recordings at nearby stations 5, 7, and Diff Array, the spectral amplitude in this frequency band grows non-linearly with increasing frequency at rates that vary from $\omega^{1/3}$ up to as high as ω^1. Accounting for possible resonant peaks at discrete frequencies, it appears that the amplitude increase is still too steep to be caused by an Airy-type caustic (two interfering rays) which would account only for an $\omega^{1/6}$ increase in spectral amplitude (Rial 1984).

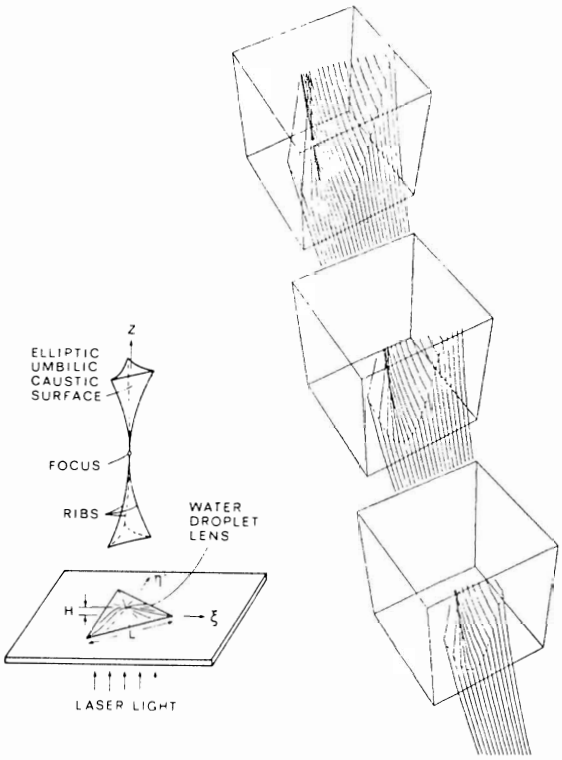

Figure 16. An alternative model of the wedge in which the intersection between the two faults is a smooth cubic function. The shape of the refracting surface is slightly modified from that used by Berry *et al.* (1979) to study the canonical elliptic umbilic caustic surface shown in the inset. The rays were traced by a 'shooting' algorithm. The three perspective cubes are located in the same geographical volume, which essentially coincides with that in Fig. 11. Thus the location of Station 6 will be near the caustic's strongest singularity (focus), which for the velocity model used is very close to the surface.

Thus, there exists the possibility that Station 6 is close to a higher order stable caustic, a cusp or an umbilic, which respectively introduce spectral amplifications of $\omega^{1/4}$ and $\omega^{1/3}$. Since the cusp is contained in the umbilic's structure, and since the wedge's geometry is topologically similar to a refractor capable of inducing an elliptic umbilic caustic (see Berry *et al.* 1979). the umbilic appears as a plausible choice.

The smoother topography of the fault intersection in the wedge given by equation (1) may be geologically justifiable, either by invoking drag folding of the Brawley fault, or folding of the deeper sediments. (Fig. 17E in Fuis *et al.* (1982) suggests the presence of smooth synclinical folding below Station 6.)

There are still other possibilities for the type of caustic affecting Station 6. The relative spectral amplitude shown in Fig. 7 in the frequency band 1–10 Hz increases on average nearly as the first power of frequency. This strong increase, if absence of contaminating effects could be proven, would suggest the presence of a point caustic, caused by the convergence of a locally spherical wavefront. This type of focusing is, however, unstable under perturbation of the control parameters (source location, velocity structure, geometry of the refractor), requiring for its appearance highly symmetric conditions not common in deformed geological structures. A slight deviation of the converging wavefront from sphericity makes the point caustic break up into stable cuspoids or umbilics.

Lack of sufficient data prevents a better assessment of what type of focusing phenomena has occurred in this area. Conservatively, it appears that an elliptic umbilic may be the correct answer.

8 Discussion and conclusions

The interpretation of the observed accelerograms presented here may not be the only one possible, but it should be clear that the particle motion orbits recorded by Station 6 are not explained by Mueller *et al.*'s (1982) model of horizontal layering in which *P*-wave reverberation or resonances have occurred. The particle motions are an important part of the data set. Any wave propagation model that attempts to explain the amplification at Station 6 has to account for the observed features of the particle motion diagrams. This argument, and our demonstration that direct *P*-waves readily focus when refracted by the Imperial Valley and Brawley faults, makes it difficult to explain amplification as the result of a cusp of the *PP*-phase. Suggested interpretations based on source effects (Archuleta 1982) lack supporting evidence. In fact, a recent study of the 23:19 aftershock of the Imperial Valley earthquake, with epicentre very close to that of the main shock, also shows strong evidence of path effects (multiple arrivals and amplification) at Station 6 (Liu & Helmberger, in preparation).

In conclusion, we propose that the largest earthquake-induced acceleration yet recorded can be interpreted as the consequence of focusing of *P*-waves refracted into the sedimentary wedge bounded by the Imperial Valley and Brawley faults. Our interpretation of the records takes into consideration the 3-D nature of the data and propagating medium. For example, 2-D ray tracing experiments would not have revealed the azimuthal convergence of ray paths which caused Station 6 to record strong *P*-phases, despite being located in the nodal direction of the *P*-wave radiation pattern.

Our results support the idea that observed large fluctuations in acceleration and ground shaking intensity can be a consequence of caustics induced by the lens-like action of sedimentary basins (Rial 1984). This idea has been extended here to include fault-bounded sediment wedges or sediment-filled depressions limited by planar fault surfaces.

The simplest possible model of the sediment wedge consists of two planar faults dipping 75° towards each other and intersecting at the surface with an included angle of 40° (Fig. 11). With this geometry, and the velocity gradient as described above, the fold caustic (codimension 1, singularity index 1/6) and the cusp (codimension 2, singularity index 1/4) can be readily formed (see Rial 1984). To explain the observed frequency behaviour at Station 6 better, a wedge model that induces the stronger elliptic umbilic caustic (codimension 3, singularity index 1/3) is proposed (Fig. 16). The possibility that local geology has induced even stronger caustics, including those of infinite codimension (e.g. a point caustic) cannot be ruled out. However, these are highly unstable catastrophes and proof of their presence would require more precise knowledge of local geology and many more observations.

Two-point boundary value solutions of the 3-D ray equations have been an invaluable tool in this research. The method, as presently implemented by Pereyra & Wojcik (1982), has provided a detailed look at the complex phenomena produced by 3-D ray refractions – with astonishing ease. Catastrophe theory, used as a background to understand and predict possible caustic structures, has been the basic conceptual guide throughout the investigation. As shown by Rial (1984), catastrophe theory provides the seismologist with a powerful tool to understand the structure of caustics produced in real geology by complex ray refractions.

Acknowledgments

The first author was supported by the US Geological Survey under Contract No. 14-08-0001-21258, and is grateful to G. Beroza and K. Bataille for their technical help and comments. The other authors were supported in part by the National Science Foundation under Lifelines Grant CEE 8116842.

References

Archuleta, R. J., 1982. Analysis of near-source static and dynamic measurements from the 1979 Imperial Valley earthquake, *Bull. seism. Soc. Am.*, **72**, 1927–1956.

Berry, M. V., Nye, J. F. & Wright, F. J., 1979. The elliptic umbilic diffraction catastrophe, *Phil. Trans. R. Soc. A*, **291**, 453–484.

Boore, D. M. & Fletcher, J. B., 1982. Preliminary study of selected aftershocks from digital acceleration and velocity recordings, in The Imperial Valley, California, earthquakes of October 15, 1979, *Prof. Pap. U.S. geol. Surv. 125A.*

Fuis, G. S., Mooney, W. D., Healy, J. H., McMechan, G. A. & Lutter, W. J., 1982. Crustal structure of the Imperial Valley region, in The Imperial Valley, California, earthquake of October 15, 1979, *Prof. Pap. U.S. geol. Surv. 254*, 25–20.

Hartzell, S. & Helmberger, D. V., 1982. Strong motion modeling of the Imperial Valley Earthquake of 1979, *Bull. seism. Soc. Am.*, **72**, 571–596.

Mueller, C. S. & Boore, D. M., 1981. Site amplifications at El Centro strong motion array Station No. 6, *Earthq. Notes*, **52**, 34.

Mueller, C. S Boore, D. M. & Porcella, R. L., 1982. Detailed study of site amplification at El Centro strong motion array Station 6, *Proc. Third int. Conf. Earthquake Microzonation*, 1, 413–424. convened Seattle, WA, 1982, June 28–July 1.

Pereyra, V., 1984. Deferred corrections software and its applications to seismic ray tracing, *Comput. Suppl.*, **5**, 211–226.

Pereyra, V. & Rial, J. A., 1981. Trazado de rayos sismicos en cuencas sedimentarias, *Acta Cient. Venezuela*, **32**, 500–502.

Pereyra, V. & Wojcik, G. L., 1982. *Two-Point Ray Tracing Software Documentation: 2-D and 3-D Codes*, Weidlinger Associates, M 8270.

Porcella, R. L. & Matthieson, R. B., 1982. Preliminary summary of the U.S. Geological Survey strong motion records from Oct. 15, 1979 Imperial Valley Earthquake, *Open File Rep. U.S. geol. Surv. No. 79-1654*, 1979.

Rial, J. A., 1984. Caustics and focusing produced by sedimentary basins: Applications of catastrophe theory to earthquake seismology, *Geophys. J. R. astr. Soc.*, **79**, 923–938.